Spectroscopic Diagnostics of Laser-Induced Titanium Plasma: Correlation of Laser Energy with Electron Temperature, Density, and Debye Shielding

Muna Ahmed Issa[1], Jenan Abdullah Khlati[1], Asmaa Mohammed Raoof[1], Shaymaa Abed Hussein[2], Sami Salman Chiad[1], Nadir Fadhil Habubi[1, 3, 4] and Yassin Hasan Kadhim[5]
[1]*Department of Physics, College of Education, Mustansiriyah University, 10052 Baghdad, Iraq*
[2]*Department of Medical Laboratory Techniques, Al-Manara College for Medical Sciences, 62001 Amarah, Iraq*
[3]*Department of Radiation and Sonar Technologies, Alnukhba University College, 10001 Baghdad, Iraq*
[4]*Department of Radiology Techniques, Al-Qalam University College, 36001 Kirkuk, Iraq*
[5]*Department of Optics Techniques, College of Health and Medical Techniques, Al-Mustaqbal University, 51001 Hillah, Iraq*
dr.sami@uomustansiriyah.edu.iq

Keywords: Titanium Plasma, LIBS, Electron Temperature, Electron Density, Debye Length, Plasma Diagnostics.

Abstract: The overall plasma parameters of the titanium plasma, including electron temperature, electron density, plasma frequency, Debye length, number of particles in the Debye sphere, and plasma coupling coefficient, were studied using laser-induced breakdown spectroscopy (LIBS). The relationship between increasing the laser energy from 400 to 700 and the plasma parameters was determined. The results showed that increasing the laser energy from 400 to 700 in steps increased the electron temperature from 0.472 to 0.500 eV (determined from a Boltzmann plot). The electron density was found to be directly proportional to increasing energy, increasing from 4.348×10^{17} to 5.797×10^{17} cm^{-3} (determined by Stark broadening). The increase in energy also raised the plasma frequency from 592.142×10^{10} to 683.726×10^{10} Hz. This is attributed to improved ablation efficiency, increased ionization, and plasma-laser interaction. With increased laser energy, the Debye length decreased from 7.74×10^{-6} to 6.90×10^{-6} cm, and the number of particles in the Debye sphere decreased from 845 to 799. This is because electrostatic potentials are screened over a shorter range, consistent with increased ionization and charge-carrier density at high ablation energies. The plasma coupling coefficient also indicated that the titanium plasma has weak coupling, as $\Gamma < 1$. The solar cell results showed that as power increased, the efficiency of the titanium films increased from 0.07% to 1.27%. These results support the possibility of controlling titanium plasma conditions by selecting laser energy and highlight the usefulness of LIBS for accurate plasma characterization.

1 INTRODUCTION

LIBS is an ever-evolving and powerful technique for elemental analysis, analyzing solids, liquids, aerosols, and gases under a broad range of experimental conditions [1]-[4]. This has made LIBS a stable and mature analytical method [5]. Titanium dioxide (TiO_2) thin films and nanoparticles have gained considerable attention for their extensive applications in electrochromic devices, photovoltaics, microelectronics, and optoelectronic systems [6]-[9]. Among metal oxide nanoparticles, TiO_2 is particularly valuable for its thermal, optical, electrical, and chemical properties [10]-[12]. TiO_2, a white, odorless, hydrophobic, stable metal oxide with remarkable opacifying potential and naturally available as titania, readily circulates [12]-[15]. Its low price, good oxidizing capacity, chemical stability, and high refractive index make it an indispensable semiconductor material across many technological domains [16]-[19]. By 2011, globally, TiO_2 nanoparticle production had surpassed 10,000 tons annually [20]. Due to its insolubility, inertness, fire resistance, wide band gap, and high surface properties [21]-[24], TiO_2's applications are numerous and wide-ranging: for dye-sensitized solar cells, self-cleaning, photocatalysis and chemical sensing systems, as well as for microelectronics, electrochemical processes, and antimicrobial applications [25]-[30]. Pulsed laser deposition (PLD) remains the most effective and controllable method for producing Ti-based thin films [31]. In PLD, a high-energy pulsed laser irradiates a solid titanium or TiO_2 target to generate a plasma plume to deposit ablated species onto a heated substrate and result in a uniform thin film [32], [33]. PLD offers several benefits, including stoichiometric transfer of target composition, fine-grain control over film thickness properties, compatibility with various gas atmospheres, and the production of high-quality nanostructured films [34], [35]. These characteristics render PLD an appealing choice for modulating the structural, optical, and functional properties of TiO_2 thin films for advanced applications [36]. While TiO_2 materials are widely studied and LIBS is an established analytical method, few studies have examined the properties of the titanium plasma generated during LIBS. Accurate measurements of plasma parameters (e.g., electron temperature (T_e), electron density (n_e), Debye length, and plasma frequency) are also essential to ensure high-efficiency ablation dynamics, enhancing emission signal quality and the accuracy of elemental analysis. However, very few works have systematically evaluated the relationship between LIBS plasma diagnostics and structural, optical, or functional properties of titanium-based materials. Thus, this study aims to fill this gap by characterizing the plasma properties of titanium resulting from LIBS ablation and how plasma-based properties affect the performance and characteristics of titanium-based thin films or nanocatalysts. This work aims to systematically investigate the plasma parameters of titanium produced by LIBS at laser pulse energies of 400, 500, 600, and 700 mJ.

2 EXPERIMENTAL

In Figure 1, the optical emission spectrum of the titanium plasma produced when it is run in air is shown using LIBS. The plasma was fabricated by a Q-switched Nd:YAG laser with a wavelength of 1064 nm, a duration of pulse of 9 ns, pulse frequency of 6 Hz, and pulse energies from 400 to 700 mJ. A concentrated laser beam was concentrated on the titanium particle at an incidence angle of 45°. The titanium plasma plume expanded above the target surface upon irradiation. Plasma light from irradiation was collected with an optical fibre at 45° to the target surface to capture additional signals and minimize geometric losses. The emission was sent to the spectrometer, where the LIBS spectra were recorded and analyzed by a computer.

A titanium sheet was used as a solid target and ablated with an Nd:YAG laser in deionized water, forming a titanium-based plasma and nanoparticles. Two laser pulse energies, 400 and 700 mJ, were chosen based on the plasma diagnostics results. Following interaction with the laser in the liquid, a transient plasma plume formed, and finally, a stable colloidal suspension of Ti-based nanoparticles was born. These nanoparticle solutions were deposited FTO glass substrates via drop-casting and then dried to obtain nanostructured thin films. The deposited layers were also thermally annealed in air to promote oxidation and develop the film's features. For the photovoltaic application, aluminum back electrodes were deposited by physical vapour deposition to complete the device structure. The newly fabricated structures were subsequently electrically contacted and characterized using current–voltage (J–V) measurements to assess their photovoltaic performance.

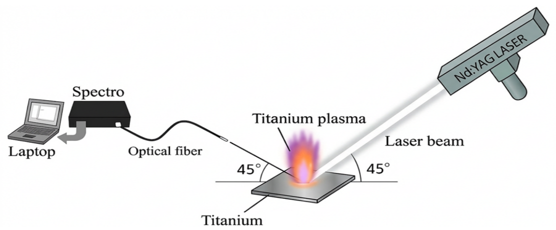

Figure 1: The LIBS system set-up.

3 RESULTS AND DISCUSSION

LIBS analysis characterizes the plasma produced from titanium during laser ablation. The laser pulse then rapidly heats and vaporizes the material, producing a dense vapor plume above the titanium surface. The laser subsequently interacts with this vapor cloud, which, in turn, leads to further ionization and a vivid plasma plume. The plasma expands and cools as it evolves, as depicted in Figure 2. These processes regulate the spectral emission characteristics obtained using LIBS measurements.

To quantitatively analyze the emission features of titanium plasma, the selected Ti spectral lines and their intensities at different laser energies were studied. Table 1 lists the standard spectroscopic parameters used in the Boltzmann analysis, including the transition probabilities (g_kA_{ki}), the lower and upper energy levels (E_i, E_j), and the characteristic wavelengths of the Ti I emission lines. Indeed, the following parameters deliver the atomic data to determine the population distribution of excited states within the plasma. The experiments have shown a range of intensities for specific Ti emission lines at laser energies of 400 to 700 mJ (Table 2). As the laser energy increases, the emission lines become stronger. This indicates higher excitation and ionization rates within the plasma. Using these intensity values is the main input required to prepare Boltzmann plots, which enable the determination of the electron temperature at each laser energy. The electron temperature, a key diagnostic parameter that reflects the electron energy distribution, provides insight into plasma excitation conditions and laser–matter interaction dynamics.

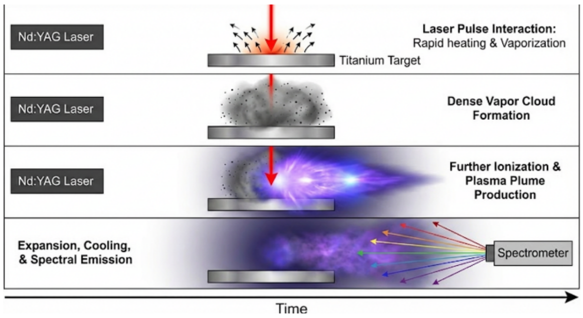

Figure 2: Stages of titanium plasma formation and emission in the LIBS process.

Table 1: Standard values of Ti.

Wavelength (nm)	$g_kA_{ki} \times 10^8$	Ei (eV)	Ej (eV)
444.9143	11	1.887	4.67301
453.3240	9.71	0.848	3.58265
461.7268	7.66	1.749	4.43335
475.8118	7.84	2.249	4.85424
499.1067	6.42	0.836	3.31943

Figure 3 shows the emission spectra of the titanium plasma generated at different laser pulse energies (400, 500, 600, and 700 mJ) in the wavelength range of 200–600 nm. A marked increase in spectral intensity occurs with increasing laser energy. For instance, at 455.25 nm, the Ti I line shows an intensity approximately 5.1 times higher than that obtained at 400 mJ. Likewise, at 323.45 nm, the Ti II line exhibits an increase of about 3.9 times for the same energy range. This increase in emission is attributable to more effective material ablation and to higher ionization intensity at higher laser energies. As the energy of the incident laser pulse increases, a greater fraction of the laser power is absorbed by the titanium surface and the expanding plasma plume. This results in higher electron temperatures, higher excitation rates, and greater collisional ionization. As a result, the plasma is denser and more emissive, yielding higher spectral lines. Such effects are consistent with the typical dynamics of laser–matter interactions previously investigated in LIBS studies [37], [38].

The Boltzmann plot method, based on both the plasma temperature and the population density of the emitting species, was employed to assess excitation and ionization processes in the plasma through spectral measurements [39]. Using multiple emission lines of the same element allows the relative population density of excited states to be estimated. But the Boltzmann method can accurately determine an excitation temperature only under local thermal equilibrium (LTE) conditions in plasma, where the level populations follow the Boltzmann distribution [10]. T_e may be obtained from the slope of the linear fit of the Boltzmann plot under LTE. Equation (1) describes the relationship used to calculate the electron temperature from measured line intensities, transition probabilities, and the energy levels of selected Ti spectral lines [15]. This temperature is an essential diagnostic index for describing the plasma energy distribution, ionization capability, and the overall dynamics of the laser–material interaction [40]:

Table 2: Observed wavelengths and their intensities of Ti at different laser energies.

400 (mJ)		500 (mJ)		600 (mJ)		700 (mJ)	
λ (nm) Observed	Intensity	λ (nm) Observed	Intensity	λ (nm) Observed	Intensity	λ (nm) Observed	Intensity
444.9143	789.623	444.9143	1139.62	444.9143	2100.94	444.9143	1686.79
454.8763	984.906	454.8763	1309.43	454.8763	2398.11	454.8763	1975.47
461.7268	271.698	461.7268	478.49	461.7268	988.68	461.7268	778.3
475.8118	280.189	475.8118	409.43	475.8118	988.68	475.8118	735.85
501.4186	653.774	501.4186	881.89	501.4186	1770	501.4186	1279.25

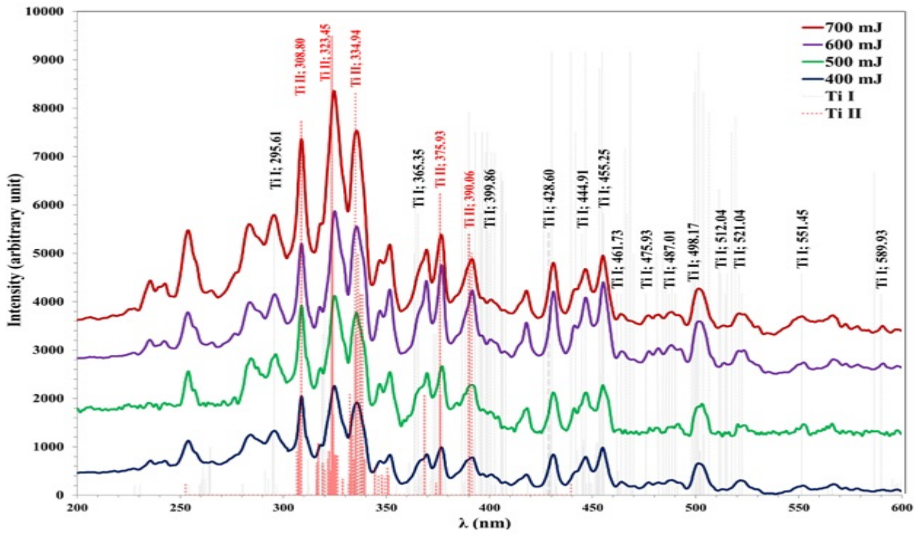

Figure 3: The emission plasma spectra of Ti generated at different laser energies.

$$\mathrm{Ln}\left(\frac{I_{ji}\lambda_{ji}}{A_{ji}g_{ji}}\right) = \frac{E_j}{k_B T_e} + C, \quad (1)$$

where I_{ji} is the relative intensity of the emission line between the energy levels i and j, λ_{ji} its wavelength, g_{ji} is the degeneracy or statistical weight of the emitting upper level i of the studied transition, and A_{ji} is the transition probability for spontaneous radiative emission from the level i to the lower level j, E_j is the excitation energy of level i, and k is the Boltzmann constant. For Boltzmann chart emission pattern, one needs multiple emission lines from the same atomic species and ionization step. Five Ti I lines at 444.91, 454.87, 461.72, 475.81, and 501.41 nm were selected for temperature determination in this study. Boltzmann plots of ln [(λ_{ij} I_{ij})/(hc A_{ij} g_j)] versus upper energy level E_j for various laser pulse energies are plotted in Figure 4. The slope of each linear fit is −1/(kB Te), which permits the electron temperature T_e to be calculated. The equations with fit and the coefficients of determination (R^2) are also shown in Figure 4; values approaching unity indicate high linearity and verify that the plasma approximates local thermal equilibrium. The calculated electron temperatures range from 0.472 to 0.500 eV, as summarized in Table 1. A larger laser pulse energy results in greater material ablation and a denser, hotter plasma. The reason is that the target surface initially absorbs a larger fraction of the incident laser energy, which is then transferred to the expanding plasma plume. The ionization and excitation rates thus increase, leading to higher emission intensities and higher kinetic energies of the plasma species. Consequently, the electron temperature rises with increasing laser energy due to typical laser-plasma interaction [41].

The electron density of the titanium plasma was determined using the Stark broadening method, which rela tes the widening of spectral lines to interactions with charged particles. According to the Stark effect, expressed in (2) [42]:

$$n_e = \left[\frac{\Delta\lambda}{2\omega_s}\right] N_r, \quad (2)$$

where ω_s is the Stark broadening parameter, Nr is the reference electron density, and Δλ is the corrected line's broadening in nm. The electron density is obtained from the full width at half maximum (FWHM) of the chosen emission line after adjusting for instrumental broadening. The Stark width ω is the theoretical broadening produced by electron–ion collisions. When charged species increase in density, perturbations to atomic energy levels become stronger, further broadening spectral lines. Therefore, Stark-induced broadening has proven to be a reasonable technique for estimating the electron density of laser-produced plasmas. Evaluated electron densities calculated from Ti I spectral lines range from 4.348×10^{17} cm^{-3} to 5.797×10^{17} cm^{-3}, showing a consistent increase with the increase in laser pulse energy. Since the ablation process is more aggressive and the ionizations are stronger, this trend results in denser plasma at higher energies. Figure 5 shows the Ti II emission line, fitted with a Lorentzian profile, in the wavelength range 308-310 nm for laser energies of 400–700 mJ. The peak intensity increases monotonically from 2.0×10^3 a.u. at 400 mJ to approximately 4.4×10^3 a.u. at 700 mJ - an

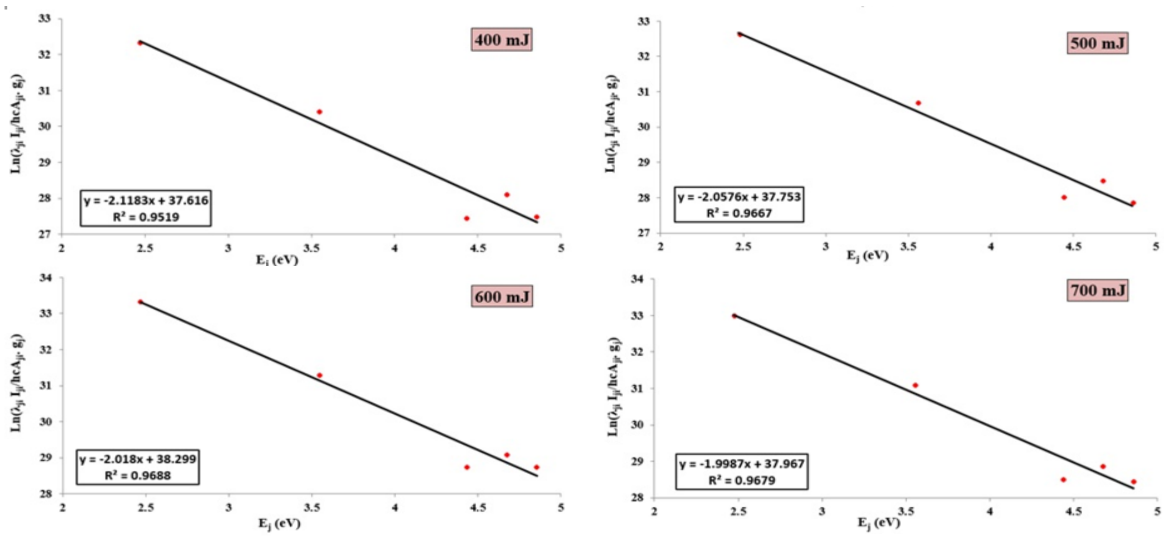

Figure 4: Boltzmann curve illustrating plasma emission from a Ti target at various laser energy levels.

enhancement factor of roughly 2.2×. Further stepwise increases in intensity at 500 and 600 mJ were consistent with this process. This systematic increase in intensity indicates better removal of the material and higher ionization and is consistent with other titanium emission lines in this work.

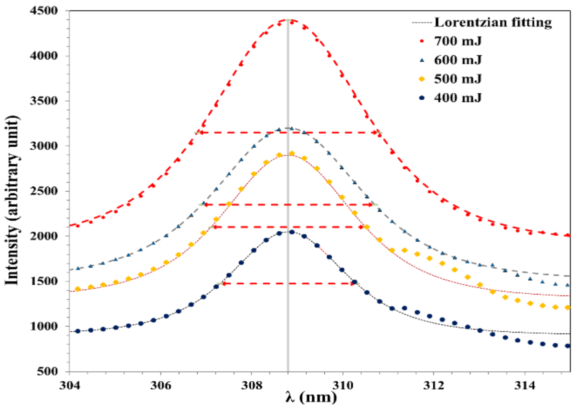

Figure 5: Stark broadening effect in Ti plasma at different laser energies.

As illustrated here, when laser pulse energy is raised, both T_e and n_e increase. Because more energetic input increases ablation rates, the vaporized material is more abundant. This increases the number of atoms excited and ionized within the plasma plume [43]. And the plasma's growing size absorbs part of the subsequent laser radiation - which is called plasma shielding - and so contributes more energy. This additional absorption increases the plasma temperature. Elevated plasma temperature increases the electron-impact ionization processes, leading to an increased number of free electrons and ultimately higher electron density [44]. Collectively, higher laser pulse energy intensifies ablation, reinforces plasma–laser interactions, and further increases thermal and collisional processes, leading to a cumulative rise in T_e and n_e.

The plasma frequency (f_p) was determined from electron density values obtained from Stark broadening analysis. The plasma frequency can be calculated using the familiar relation [45], [46].

$$f_p\ (Hz) = 8.98 \times 10^3 \sqrt{n_e}\,. \quad (3)$$

This means that the plasma frequency is directly proportional to the square root of the electron density. Such a pattern is observed in Table 3 and shown in Figure 6 below, where the plasma frequency rises monotonically with laser pulse intensity. Because of this, the electron density is greatly increased at high ablation energies, and the plasma frequency is directly proportional to the square root of the electron density. The resultant increase in f_p is evidenced by the enhancement of the collective electron response and the appearance of higher plasma oscillations at high laser doses [47], [48].

In a plasma, charged particles collectively shield the Influence of external electric fields through a process called Debye shielding. The collective behaviour we see in this case maintains the plasma's quasi-neutrality, with the overall densities of positive and negative charges remaining, on macroscopic scales, almost equal. The size of screening of electric potentials is defined as the Debye length (λ_D), which is the fundamental depth to which electrostatic perturbations are considerably lessened [49], [50]. For Debye shielding to be relevant, the plasma must meet certain criteria. In general, a necessary number of electrons must be present in a spherical zone of radius λ_D, a region of the plasma known as the Debye sphere. The number of particles in this sphere, called the Debye number (N_D), is one of the key criteria to establish the medium as a real plasma. $N_D \gg 1$ is normally present for a plasma so that many charged particles are involved in this shielding process. Both Debye length and Debye number depend directly on T_e and n_e (Fig. 7). Higher electron temperatures increase electron thermal motion and thus lead to larger Debye lengths. Yet, greater electron density makes the plasma's ability to protect electric fields increase, so that λ_D decreases instead of increasing [51], [52].

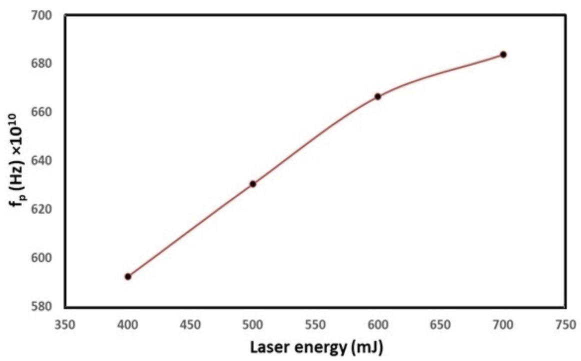

Figure 6: The relation between plasma frequency and different laser energies.

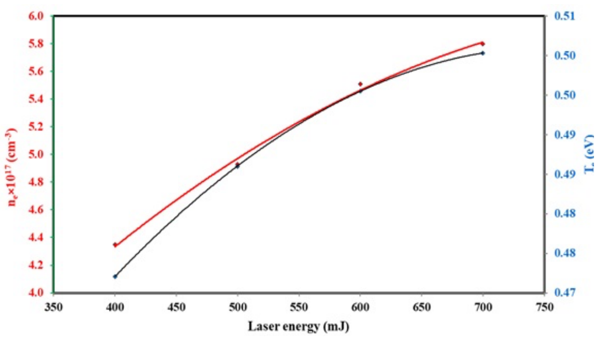

Figure 7: Relations between T_e, n_e, and different laser energies.

These relationships are described mathematically by (4) and (5) [53], [54]:

$$\lambda_D = \sqrt{\frac{\varepsilon_0 K_B T_e}{n_e e^2}}, \tag{4}$$

$$N_D = \frac{4\pi}{3} n_e \lambda_D^3. \tag{5}$$

The degree of both plasma temperature and electron density is crucial for determining Debye length and Debye number. As shown in Table 3, higher laser pulse energy leads to a slight increase of T_e and a significant increase in electron density. Due to the inverse correlation between electron density and λ_D, the higher plasma density at higher laser energies will result in a significantly lower λ_D. Indeed, the length of Debye length varies from 7.74×10^{-6} cm at 400 mJ to 6.90×10^{-6} cm at 700 mJ. This reduction in λ_D directly changes the size of the Debye sphere and, with it, the Debye Number (N_D), which decreases from a value of 845 to 799 as the laser energy increases. Although the decrease in N_D is small, it reflects a stronger, denser combined plasma environment [55], [56]. A decrease in the Debye suggests that electrostatic potentials are screened over a shorter distance, consistent with enhanced ionization and increased charge-carrier density at higher ablation energies. Such behaviour is consistent with the formation of a more compact, strongly interacting plasma plume as the laser energy increases [57], [58].

To further quantify the strength of interparticle interactions in the plasma, we measured the plasma coupling parameter (Γ). This parameter relates the Coulomb interaction energy in the plasma between the charged particles to their thermal kinetic energy [59], [60]:

$$\Gamma = \frac{e^2}{4\pi\, \varepsilon_0 a k_B T_e}. \tag{6}$$

where e is the elementary charge, ε_0 is the vacuum permittivity, k_B is the Boltzmann constant, T_e is the electron temperature, and a is the average interparticle distance (Wigner–Seitz radius), defined as [61]:

$$a = \left(\frac{3}{4\pi n_e}\right)^{\frac{1}{3}}. \tag{7}$$

Following the general decrease in the Debye length and Debye number described earlier, as the n_e increases with laser pulse energy, the mean interparticle spacing decreases, augmenting Coulomb interactions and, over time, raising the plasma coupling parameter, as shown in Figure 8. At the same time, the calculated Γ values were less than unity at all energies studied, indicating that the plasma has weakly coupled behaviour. This behaviour is fully consistent with the Debye analysis, confirming the interpretation of a denser, but non-strongly coupled, plasma plume at higher ablation energies [62].

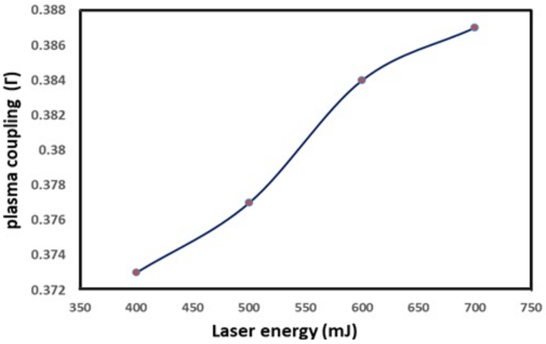

Figure 8: Variation of the plasma coupling parameter (Γ) as a function of laser pulse energy [63].

The uncertainties associated with the calculated plasma parameters, T_e, n_e, λ_D, and N_D were evaluated by accounting for fluctuations in laser pulse energy (±5%) and spectral fitting errors arising from the Boltzmann and Stark analyses. The estimated uncertainty in the electron temperature is approximately ±0.02 eV. In contrast, the electron density carries an uncertainty of about $\pm 0.3 \times 10^{17}$ cm^{-3}, primarily due to variations in the Stark broadening measurements and fitting precision. Since the Debye length depends on both T_e and n_e, its propagated uncertainty is somewhat larger, on the order of $\pm 0.4 \times 10^{-6}$ cm. This reflects the combined Influence of uncertainties in temperature and density on the electrostatic screening distance. Consequently, the Debye number N_D, which scales with λ_D^3, exhibits an even more pronounced propagated uncertainty of roughly 20%. The uncertainty in the plasma coupling parameter (Γ) was calculated using standard error propagation, given its dependence on electron temperature and density [64], [65]. Consequently, the uncertainty of Γ is found to be on the order of 6–8% so that the plasma is classified as weakly coupled (Γ < 1) [66]. J–V profiles of the Ti-based photovoltaic devices (400 mJ and 700 mJ of laser pulse energies) are depicted in Figures 9 and 10. The electrical properties of TiO_2 and Si were used in a solar cell, as shown in Table 4. A comparison was made between the results in 400 mJ and 700 mJ. They observed higher solar cell efficiency at higher laser energy and found the highest efficiency for the TiO_2 cell film at E=400 mJ (0.07%) and E=700 mJ (1.27%). This is because increased energy improves film homogeneity and density, as reported by [67]. The best results were at a laser energy of 700 mJ.

Table 3: Plasma parameters for Ti plasma at different laser energies.

E (mJ)	T_e (eV)	$n_e \times 10^{17}$ (cm^{-3})	f_p (Hz) $\times 10^{10}$	$\lambda_D \times 10^{-6}$(cm)	N_d	A (nm)	Γ
400	0.472	4.348	592.124	7.74	845	8.19	0.373
500	0.486	4.928	630.364	7.38	829	7.85	0.377
600	0.496	5.507	666.413	7.05	808	7.57	0.384
700	0.500	5.797	683.726	6.90	799	7.44	0.387

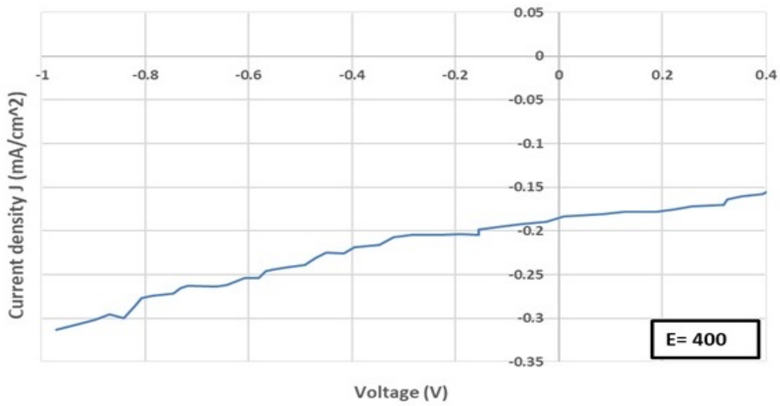

Figure 9: I-J diagram of the Silicon solar Cell at E=400 mj.

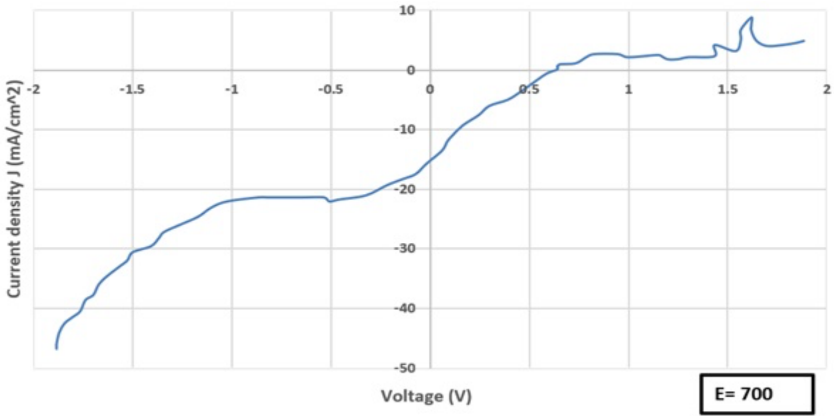

Figure 10: I-J diagram of the Silicon solar Cell at E=700 mj.

Table 4: Solar cell parameters measurements.

E (mJ)	PCE (%)	FF (%)	Jsc (mA.cm^{-2})	Voc (V)
400	0.07	44.77	-0.18	0.856
700	1.27	19.51	-12.56	0.519

4 CONCLUSIONS

Based on a comprehensive spectroscopic analysis of titanium plasma, a clear relationship is observed between increasing laser energy, plasma parameters, and solar cell efficiency. As the laser energy increases from 400 to 700 mJ, several significant changes occur. First, the emission lines of Ti I and Ti II become more clearly resolved in the recorded spectra. Second, both the electron temperature and electron density increase with rising laser energy. This direct correlation indicates that the plasma conditions of titanium can be effectively controlled to improve diagnostic performance using the Laser-Induced Plasma Spectroscopy (LIPS) technique. In addition, the Debye length and the number of particles within the Debye sphere decrease with increasing laser energy. Meanwhile, the coupling coefficient increases, suggesting that the titanium plasma operates within a weakly coupled regime. Furthermore, a noticeable improvement in solar cell efficiency is observed as the laser energy increases. These results demonstrate that titanium plasma conditions can be effectively controlled through careful adjustment of laser energy, and they further emphasize the capability of Laser-Induced Breakdown Spectroscopy (LIBS) as a reliable and precise diagnostic tool for plasma characterization.

ACKNOWLEDGMENTS

This research was backed by Mustansiriyah University (www.uomustansiriyah.edu.iq) through its institutional academic research program.

REFERENCES

[1] M. Vasudeva, S. D. Varalakshmi, S. D. George, and V. K. Unnikrishnan, “Engineered liquid-repellent substrate for enhanced Laser-Induced Breakdown Spectroscopy (LIBS) of liquid samples,” Applied Surface Science, article no. 166364, 2026.

[2] B. Xue, W. Sun, Y. Bai, Z. Wang, C. Chen, X. X. Li,and Y. You, “Laser energy modulation in laser-induced breakdown spectroscopy of marine aerosols: unraveling energy-coupling pathways and improving quantitative analysis,” Journal of Analytical Atomic Spectrometry, 2026.

[3] Y. You, B. Xue, and J. Riedel, “Enhancement of LIBS plasma in air with organic solvent vapors,” Spectrochimica Acta Part B: Atomic Spectroscopy, vol. 236, article no. 107309, 2026.

[4] J. Li, Y. Zhang, C. Zhang, D. He, X. Cheng, and J. Bai, “Gas or bulk?- size effect of aerosol particles in interaction with laser-induced plasma,” Optics & Laser Technology, vol. 193, article no. 114245, 2026.

[5] A. P. Sreekala, D. B. Mora, M. B. de la Mora Mojica, J. Y. T. Sánchez, V. Contreras, and C. Sánchez-Aké, “Laser-induced breakdown spectroscopy of water-dispersed gold nanoparticles in acoustically levitated droplets: Parameter adjustment for enhanced signal,” Spectrochimica Acta Part B: Atomic Spectroscopy, article no. 107483, 2026.

[6] H. Enayati-Taloobaghi, S. Soltani, M. M. Shahidi, and E. Salahi, “Phase engineering and UV photoresponse of TiO_2 films on Si substrates modified with spatially distributed Au nanoparticles,” Journal of Materials Science: Materials in Electronics, vol. 37, no. 2, p. 155, 2026.

[7] C. Z. Eldjilali, G. S. H. Thien, Z. N. Ng, B. K. Yap, K. B. Tan, H. A. Murthy, and K. Y. Chan, “Electrochromic performances of TiO_2 nanocrystals thin films for smart glass applications,” Thin Solid Films, vol. 815, article no. 140636, 2025.

[8] M. K. Rashid, H. J. Mohammed, H. M. Hameed, M. W. Muayad, A. M. Hussien, A. T. Awad, and M. Alharbi, “The effect of titanium dioxide (TiO_2) nanoparticle concentration on the performance of polycrystalline silicon solar cells,” Journal of Umm Al-Qura University for Engineering and Architecture, vol. 16, no. 4, pp. 1753-1764, 2025.

[9] R. Özmenteş and A. S. Hassanien, “Characterizations and optical discussions of thermally evaporated titanium dioxide thin films,” Journal of Optics, vol. 54, no. 3, pp. 1322-1340, 2025.

[10] A. M. Al Saleh, “A Review of the Synthesis, Structural, and Optical Properties of TiO_2 Nanoparticles: Current State of the Art and Potential Applications,” Crystals, vol. 15, no. 11, p. 944, 2025.

[11] İ. Erol, G. Khamidov, R. Uktamjon, T. Davlat, and S. Tillayev, “Enhanced thermal, dielectric, and antimicrobial performance of fluorinated methacrylate and chitosan-based nanocomposites reinforced with TiO_2 nanowires,” Cellulose, vol. 32, no. 16, pp. 9429-9450, 2025.

[12] M. A. Issa and K. A. Aadim, “Optical and structural characterization of ZnO:NiO nano composite prepared by pulsed laser deposition method,” J. Opt., vol. 54, pp. 2357-2362, 2025.

[13] M. L. Vera, H. D. Traid, A. N. Dwojak, M. R. Rosenberger, and C. E. Schvezov, “Advances in nanostructured TiO_2 coatings for industrial applications,” in Industrial Applications of Nanoparticles. CRC Press, pp. 228-255, 2023.

[14] K. Nagaraj, S. Radha, C. G. Deepa, K. Raja, V. Umapathy, N. P. Badgujar,and C. Uthra, “Photocatalytic advancements and applications of titanium dioxide (TiO_2): Progress in biomedical, environmental, and energy sustainability,” Next Research, vol. 2, no. 1, article no. 100180, 2025.

[15] N. Farooq, P. Kallem, Z. ur Rehman, M. I. Khan, R. K. Gupta, T. Tahseen,and A. Shanableh, “Recent trends of titania (TiO_2) based materials: A review on synthetic approaches and potential applications,” Journal of King Saud University-Science, vol. 36, no. 6, article no. 103210, 2024.

[16] N. S. Kamarudin, N. N. Yaakob, N. F. Sukor, H. D. Setiabudi, M. A. H. Aziz, and R. Jusoh, “Dual-Role Deep Eutectic Solvent-Assisted Electrosynthesis of TiO_2/KCC-1 for Enhanced Visible-Light Photocatalytic Desulfurization,” Arabian Journal for Science and Engineering, pp. 1-20, 2026.

[17] W. Zhao, H. Jia, J. Qu, C. Yang, Y. Wang, J. Zhu,and G. Liu, “Sol-gel synthesis of TiO_2-SiO_2 hybrid films with tunable refractive index for broadband antireflective coatings covering the visible range,” Journal of Sol-Gel Science and Technology, vol. 107, no. 1, pp. 105-121, 2023.

[18] M. O’Byrne, B. Kerzabi, M. Abbarchi, A. Lifschitz, T. Zamora, V. Malgras,and M. Putero, “Investigation of the anatase-to-rutile transition for TiO_2 sol-gel coatings with refractive index up to 2.7,” Thin Solid Films, vol. 790, article no. 140193, 2024.

[19] A. Saeed, E. Alzahrani, M. A. Morsi, A. E. Tarabiah, E. M. Abdelrazek, S. Aldwais,and A. A. Al-Muntaser, “Enhanced optical and electrical properties of PEO/PMMA/TiO_2 nanocomposites for optoelectronic applications,” Optical Materials, vol. 157, article no. 116402, 2024.

[20] F. Piccinno, F. Gottschalk, S. Seeger, and B. Nowack, “Industrial production quantities and uses of ten engineered nanomaterials in Europe and the world,” Journal of Nanoparticle Research, vol. 14, no. 9, p. 1109, 2012.

[21] K. A. D. H. I. M. Al-Attafi and R. K. Naser, “A Review on Reducing TiO_2 Photocatalysis in Sunscreens: Perspectives on TiO_2@Zn_2SnO_4 Composites,” Journal of Kerbala University, vol. 22, no. 4, pp. 72-90, 2025.

[22] J. B. Mbaluka, “Surface Roughness, Band Gap, Crystallite Size and Surface Potential Tuning and Their Effect on Photocatalytic Activity of Titanium Dioxide Thin Films,” Doctoral dissertation, JKUAT-COPAS, 2022.

[23] P. A. Salazar, C. L. Fernández, Y. Luna-Galiano, R. V. Sánchez, and C. Fernández-Pereira, “Physical, mechanical and radiological characteristics of a fly ash geopolymer incorporating titanium dioxide waste as passive fire insulating material in steel structures,” Materials, vol. 15, no. 23, p. 8493, 2022.

[24] M. Hajihashemi, M. Shamanian, and F. Ashrafizadeh, “Band gap tuning of oxygen vacancy-induced Al_2O_3-TiO_2 ceramics processed by spark plasma sintering,” Journal of Electroceramics, vol. 48, no. 1, pp. 35-50, 2022.

[25] B. Senthil Rathi, L. S. Ewe, S. S, S. S, W. K. Yew, B. R, and S. K. Tiong, “Recent trends and advancement in metal oxide nanoparticles for the degradation of dyes: synthesis, mechanism, types and its application,” Nanotoxicology, vol. 18, no. 3, pp. 272-298, 2024.

[26] G. Kaur, P. Negi, R. J. Konwar, H. Kumar, N. Devi, G. Kaur,and A. N. Yadav, “Tailored TiO_2 nanostructures for designing of highly efficient dye sensitized solar cells: a review,” Nano-Structures & Nano-Objects, vol. 36, article no. 101056, 2023.

[27] Q. Yuan, C. Shi, and T. He, “SiO_2/TiO_2 and PDMS modified self-cleaning coating and its application in decorative UHPC surface,” Ceramics International, vol. 50, no. 4, pp. 6194-6206, 2024.

[28] T. Cao, W. Dong, Y. Liang, Q. Bao, C. Xu, M. Bai,and X. Gu, “A simple solvothermal preparation of Mg-doped anatase TiO_2 and its self-cleaning application,” Solar Energy, vol. 249, pp. 12-20, 2023.

[29] A. Shadab and S. K. Raghuwanshi, “Development and sensitivity analysis of rGO-TiO_2 coated eFBG sensor for the detection of ethanol in petrochemicals,” IEEE Sensors Journal, vol. 22, no. 13, pp. 12913-12920, 2022.

[30] S. Devi, N. Talreja, D. Chauhan, S. Sahu, and M. Ashfaq, “Bioresource-derived Propolis wrapping for ZnO/TiO_2 nanocomposites: A sustainable photo-antibiotic material,” Inorganic Chemistry Communications, article no. 116270, 2026.

[31] M. A. Issa and K. A. Aadim, “Influence Of Laser Energy On Structural And Optical Properties Of ZnO(x):NiO(1−x) Films Prepared By Pulse Laser Deposition,” J. Opt., 2024.

[32] S. N. Ogugua, O. M. Ntwaeaborwa, and H. C. Swart, "Latest development on pulsed laser deposited thin films for advanced luminescence applications," Coatings, vol. 10, no. 11, p. 1078, 2020.

[33] H. R. Humud and T. A. Hameed, "Studying the physicochemical properties of water activated by cold atmospheric plasma jet," Iraqi Journal of Science, pp. 4748-4756, 2024.

[34] L. Duta and A. C. Popescu, "Current status on pulsed laser deposition of coatings from animal-origin calcium phosphate sources," Coatings, vol. 9, no. 5, p. 335, 2019.

[35] M. A. Issa and K. A. Aadim, "Study the structural and optical properties of Zinc Oxide prepared by pulse laser deposition," J. Opt., 2024.

[36] Olvera-Rodríguez, R. Hernández, A. Medel, C. Guzmán, L. Escobar-Alarcón, E. Brillas,and K. Esquivel, "TiO_2/Au/TiO_2 multilayer thin-film photoanodes synthesized by pulsed laser deposition for photoelectrochemical degradation of organic pollutants," Separation and Purification Technology, vol. 224, pp. 189-198, 2019.

[37] Liu, D. Wu, X. Hu, S. Liu, H. Wu, R. Hai,and H. Ding, "Study of spectral intensity of the laser ablated tungsten plasma and ablation mass at various laser spot sizes and laser fluence in vacuum environment," Spectrochimica Acta Part B: Atomic Spectroscopy, vol. 199, article no. 106569, 2023.

[38] A. Yahya, "Enhancement of electron temperature under dense homogenous plasma by pulsed laser beam," Baghdad Science Journal, vol. 18, no. 4, p. 23, 2021.

[39] A. Safi, S. H. Tavassoli, G. Cristoforetti, S. Legnaioli, V. Palleschi, F. Rezaei, and E. Tognoni, "Determination of excitation temperature in laser-induced plasmas using columnar density Saha-Boltzmann plot," Journal of Advanced Research, vol. 18, pp. 1-7, 2019.

[40] S. N. T. AlRashid, S. N. Mazhir, and N. M. Hamid, "Spectroscopic Investigation of Plasma Parameters in an CdO Target Using Laser-Induced Breakdown Spectroscopy," Journal of Physical Science, vol. 36, no. 3, pp. 75-87, 2025.

[41] Y. Dong, L. Su, Y. Liao, W. Li, C. Wu, Q. Wang,and W. Guo, "Investigation of molten spattering and plasma evolution in femtosecond laser ablation of superalloy," Journal of Manufacturing Processes, vol. 151, pp. 595-606, 2025.

[42] Issa and K. A. Aadim, "Influence of gas flow rate on the plasma temperature and electron density of an atmospheric argon plasma jet," Jordan Journal of Physics, vol. 18, no. 4, pp. 435-442, 2025.

[43] A. M. Mostafa, "The Influence of various parameters on the ablation and deposition mechanisms in pulsed laser deposition," Plasmonics, pp. 1-19, 2025.

[44] R. Chatterjee, "Fundamental concepts and discussion of plasma physics," TECHNO REVIEW Journal of Technology and Management, vol. 2, no. 1, pp. 01-14, 2022.

[45] Q. A. Abbas, "Effect of Target properties on the Plasma Characteristics that produced by Laser at Atmospheric Pressure," Iraqi Journal of Science, pp. 1251-1258, 2019.

[46] H. Ahmed and H. R. Humud, "The Influence of Gas Type and Flow Rate on Plasma Jet Length and Gas Temperature," Iraqi Journal of Physics, vol. 23, no. 3, pp. 128-136, 2025.

[47] E. S. Hassan, A. K. Elttayef, S. H. Mostafa, M. H. Salim, and S. S. Chiad, "Silver oxides nanoparticle in gas sensors applications," Journal of Materials Science: Materials in Electronics, vol. 30, no. 17, pp. 15943-15951.

[48] S. K. Muhammad, E. S. Hassan, K. Y. Qader, K. H. Abass, S. S. Chiad, and N. F. Habubi, "Effect of vanadium on structure and morphology of SnO_2 thin films," Nano Biomedicine and Engineering, vol. 12, no. 1, pp. 67-74, 2020.

[49] D. A. Cremers and L. J. Radziemski, Handbook of Laser-Induced Breakdown Spectroscopy, 2nd ed. Chichester, U.K.: Wiley, 2013.

[50] Dhankhar, O. P. Singh, and V. N. Singh, "Physical principles of losses in thin film solar cells and efficiency enhancement methods," Renewable and Sustainable Energy Reviews, vol. 40, pp. 214-223, 2014.

[51] G. Lu, L. Sun, Z. Cong, and T. Chen, "Study on laser-induced breakdown spectroscopy in high-pressure helium gas environment for deep ocean applications," Talanta, vol. 270, article no. 125531, 2024.

[52] C. Ghany, K. M. Lee, H. K. Sanghapi, and V. K. Singh, "Diagnostics of Laser-Induced Plasma," in Laser Induced Breakdown Spectroscopy (LIBS): Concepts, Instrumentation, Data Analysis and Applications, vol. 1, pp. 45-64, 2023.

[53] Z. J. Kamil, M. J. Zoory, and H. J. Mohamad, "LIBS technique for plant mineral ratio analysis and environmental and agricultural importance: a comprehensive review," The European Physical Journal D, vol. 78, no. 3, p. 27, 2024.

[54] A. V. Skalny, T. V. Korobeinikova, M. Aschner, O. V. Baranova, E. G. Barbounis, A. Tsatsakis, and A. A. Tinkov, "Medical application of laser-induced breakdown spectroscopy (LIBS) for assessment of trace element and mineral in biosamples: Laboratory and clinical validity of the method," Journal of Trace Elements in Medicine and Biology, vol. 79, article no. 127241, 2023.

[55] T. K. Sankar, Abhilash, and P. Meshram, "Environmental impact assessment in the entire life cycle of lithium-ion batteries," Reviews of Environmental Contamination and Toxicology, vol. 262, no. 1, p. 5, 2024.

[56] G. S. Senesi and R. S. Harmon, "Application of LIBS to terrestrial geological research," in Laser Induced Breakdown Spectroscopy (LIBS): Concepts, Instrumentation, Data Analysis and Applications, vol. 2, pp. 593-614, 2023.

[57] V. Balaram, "Advances in analytical techniques and applications in exploration, mining, extraction, and metallurgical studies of rare earth elements," Minerals, vol. 13, no. 8, p. 1031, 2023.

[58] A. G. Ramu, M. A. Kumari, J. Theerthagiri, D. Choi, and M. Y. Choi, "Metal nanoparticles and alloys produced by pulsed laser irradiation in liquids for water splitting," in Pulsed Laser-Induced Nanostructures in Liquids for Energy and Environmental Applications. Elsevier, pp. 177-191, 2024.

[59] Y. Liu, C. Wu, L. Dong, and J. Xiu, “Multi-dimensional analysis of NiCr alloy nanofilms based on Ps-LIBS technology,” Spectrochimica Acta Part B: Atomic Spectroscopy, vol. 222, article no. 107062, 2024.
[60] T. Weiland and I. Williams, “Culturally relevant data in teaching statistics and data science courses,” Journal of Statistics and Data Science Education, vol. 32, no. 3, pp. 256-271, 2024.
[61] D. A. Cremers and L. J. Radziemski, Handbook of Laser-Induced Breakdown Spectroscopy, 2nd ed. Chichester, U.K.: Wiley, 2013.
[62] J. Clérouin, G. Robert, P. Arnault, J. D. Kress, and L. A. Collins, “Behavior of the coupling parameter under isochoric heating in a high-Z plasma,” Physical Review E: Statistical, Nonlinear, and Soft Matter Physics, vol. 87, no. 6, article no. 061101, 2013.
[63] A. Inogamov, Y. V. Petrov, V. A. Khokhlov, and V. V. Zhakhovskii, “Laser ablation: physical concepts and applications,” High Temperature, vol. 58, no. 4, pp. 632-646, 2020.
[64] H. Naser, M. A. Alghoul, M. K. Hossain, N. Asim, M. F. Abdullah, M. S. Ali,and N. Amin, “The role of laser ablation technique parameters in synthesis of nanoparticles from different target types,” Journal of Nanoparticle Research, vol. 21, no. 11, p. 249, 2019.
[65] N. Ali, S. Bashir, A. M. Alshehri, and N. Begum, “Study of micro/nano structuring and mechanical properties of KrF excimer laser irradiated Al for aerospace industry and surface engineering applications,” Materials, vol. 14, no. 13, p. 3671, 2021.
[66] J. Zhang, J. Claverie, M. Chaker, and D. Ma, “Colloidal metal nanoparticles prepared by laser ablation and their applications,” ChemPhysChem, vol. 18, no. 9, pp. 986-1006, 2017.
[67] H. O. Hussein and W. I. Yaseen, “Plasma optical emission spectroscopy study of some iron meteorites,” Iraqi Journal of Science, pp. 2925-2933, 2024.